Article

Rh#Pt Bimetallic Catalysts: Synthesis, Characterization, and Catalysis of Core#Shell, Alloy, and Monometallic Nanoparticles

Selim Alayoglu, and Bryan Eichhorn

J. Am. Chem. Soc., **2008**, 130 (51), 17479-17486 • DOI: 10.1021/ja8061425 • Publication Date (Web): 02 December 2008

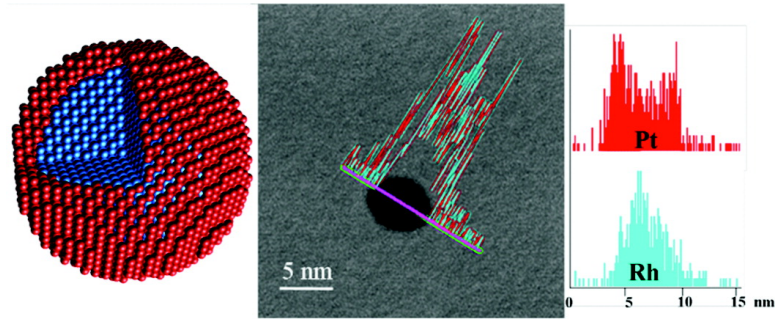

More About This Article

Additional resources and features associated with this article are available within the HTML version:

- Supporting Information
- Access to high resolution figures
- Links to articles and content related to this article
- Copyright permission to reproduce figures and/or text from this article

View the Full Text HTML

J|A|C|S
ARTICLES

Published on Web 12/02/2008

Rh−Pt Bimetallic Catalysts: Synthesis, Characterization, and Catalysis of Core−Shell, Alloy, and Monometallic Nanoparticles

Selim Alayoglu and Bryan Eichhorn*

Department of Chemistry and Biochemistry, University of Maryland, College Park, Maryland 20742

Received August 5, 2008; E-mail: eichhorn@umd.edu

Abstract: Rh@Pt core−shell, RhPt (1:1) alloy, and Rh + Pt monometallic nanoparticles (NPs) were prepared using standard polyol reduction chemistry in ethylene glycol (EG) with standard inorganic salts and polyvinylpyrrolidine (PVP_{55000}) stabilizers. PVP-free colloids were also prepared but less stable than the PVP-protected NPs. Rh@Pt core−shell particles were prepared from 2.7, 3.3, and 3.9 nm Rh cores with varying shell thicknesses (∼1 and ∼2 ML). The particles were characterized by a combination of TEM, single-particle EDS, EDS line scans, XRD analysis, Debye Function simulations, FT-IR, and micro-Raman CO-probe experiments. The three different architectures were evaluated for preferential oxidation of CO in hydrogen (PROX) using 1.0 wt % Pt loadings in Al_2O_3 supports. For hydrogen feeds with 0.2% CO and 0.5% O_2 the Rh@Pt NP catalyst has the best activity with complete CO oxidation at 70 °C and very high PROX selectivity at 40 °C with 50% CO conversion.

Introduction

Rodriguez, Goodman, and others[1−3] performed detailed studies of metal thin film overlayers deposited on bulk metallic surfaces. The studies were designed to probe the electronic structures and nature of metal−metal bonding between the metal overlayers and the metallic substrates. The results showed that work functions of metallic films were altered from their bulk values due to the structural and electronic effects of the underlying metal host. Through a combination of thermal desorption studies and photoelectron experiments the studies documented significant intermetallic electron transfers between overlayer and substrate metals having different d-band electronic populations. In general, it was shown that electron density was transferred from those metals with filled d states to those with less filled d states. These findings differ from the electronic interactions in bulk intermetallics and alloys where electronegativity considerations dictate the magnitude and direction of electron transfer. More recent studies[3−8] have shown that lowering the energy of the metal overlayer's d-band center has a significant impact on the interactions of the metal overlayer with adsorbate molecules on the surface. The resulting changes in activation energies and bond enthalpies of adsorbates have dramatic effects on the catalytic activities. For example, Mavrikakis et al. have shown[8,9] that hydrogen-bond enthalpies on Pt monolayers were reduced by as much as 0.4 eV depending on the substrate, which makes them far more active for hydrogenation than bulk Pt. In a study of Pt overlayers on Ru(0001) hosts Jakob and co-workers elegantly showed how the structural and electronic influences of the host could be experimentally differentiated.[3] They showed that the electronic influence of the host Ru metal on the Pt overlayer was maximized with single monolayer films but quickly disappeared after three or more monolayers of coverage. In contrast, the structural influences of the substrate persisted to greater overlayer thickness due to long-range pseudomorphic growth.[3]

Translation of these results from bulk monolayer surface structures to nanoparticles (NPs) with monolayer shells on metallic cores (i.e., M@M′ core−shell NPs, see drawing) is not completely obvious. For example, how will deviations from bulk band structures and finite electronic states affect charge transfer between the core and shell metals? How will the surface strain of the shell of a core−shell NP compare to that of a bulk thin film overlayer grown pseudomorphically on a faceted substrate? Mavrikakis and co-workers developed remarkably accurate "near surface alloy" theoretical models for describing trends in activity, adsorbate binding, and mechanistic pathways on various core−shell structures.[9] However, several approximations must be made in order to perform such detailed analysis on these large, complicated systems. The approximations, such as perfectly faceted substrates and uniform interfaces between core and shell metal layers, may cause complications in modeling nonuniform, multifaceted core−shell NPs made from solution. It is clear that additional comparative experimental investigations of core−shell and alloy NP systems are needed

(1) Rodriguez, J. A.; Goodman, D. W. *Science* **1992**, *257*, 897–903.
(2) Campbell, C. T. *Annu. Rev. Phys. Chem.* **1990**, *41*, 775–837.
(3) Schlapka, A.; Lischka, M.; Gross, A.; Kasberger, U.; Jakob, P. *Phys. Rev. Lett.* **2003**, *91*, 016101/1−016101/4.
(4) Jakob, P.; Schlapka, A. *Surf. Sci.* **2007**, *601*, 3556–3568.
(5) Rodriguez, J. A.; Campbell, R. A.; Goodman, D. W. *J. Phys. Chem.* **1991**, *95*, 5716–5719.
(6) Rodriguez, J. A.; Campbell, R. A.; Goodman, D. W. *J. Phys. Chem.* **1990**, *94*, 6936–6939.
(7) Rodriguez, J. A.; Campbell, R. A.; Goodman, D. W. *J. Vac. Sci. Technol. A* **1991**, *9*, 1698–1702.
(8) Greeley, J.; Krekelberg, W. R.; Mavrikakis, M. *Angew. Chem., Int. Ed.* **2004**, *43*, 4296–4300.
(9) Greeley, J.; Mavrikakis, M. *Nat. Mater.* **2004**, *3*, 810–815.

to unravel the underlying structural and electronic principles governing the activities of bimetallic nanoparticles and help refine modeling studies.

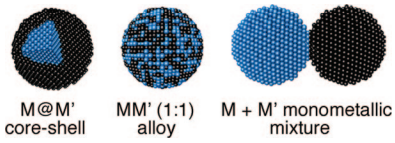

While some bimetallic NP catalysts show expected and somewhat systematic changes, other systems are less predictable and have surprising activities. For example, CO oxidation catalyzed by $Pt_{1-x}Rh_x$ alloy NPs show activities intermediate to those of the Pt and Rh NP end members.[10] In contrast, preferential oxidation of CO in hydrogen (PROX) activities of the $Pt_{1-x}Ru_x$ NPs are much better than those of the Pt and Ru end members due to synergistic effects of the alloy surfaces. Moreover, the Ru@Pt core−shell NPs are far superior to the $Pt_{1-x}Ru_x$ alloy NPs and monometallic mixtures.[11] To experimentally probe the importance of architecture in bimetallic NP systems we embarked on a systematic evaluation of bimetallic particles in different architectural configurations, namely, core−shell, alloy, and mixed monometallic NPs (see drawing). We report here the full synthetic, spectroscopic, and structural characterization of Rh@Pt core−shell NPs with different core sizes and shell thicknesses with and without surfactant stabilizers. In addition, our preliminary catalysis studies show that the Rh@Pt core−shell NPs are superior to the alloy and monometallic mixtures for PROX applications. Full catalytic evaluations and theoretical studies will be reported in a subsequent publication.

Experimental Section

All reactions were carried out under N_2 atmosphere using standard Schlenk line techniques on a Fisher Scientific Isotherm hot plate stirrer with a temperature control unit using a Teflon-coated K-type thermocouple. Chemicals, $PtCl_2$ (Engelhard, Pt 73.09%), $Pt(acac)_2$ (Strem, 98%, acac = acetylacetonate), $Rh(NO_3)_3 \cdot 2H_2O$ (Alfa Aesar, 99.9% pure, Rh 31.1%), $RhCl_3$ (Engelhard, Rh 39.46%), $Rh_2(CO)_4Cl_2$ (Fluka, >97%), polyvinylpyrrolidine (Aldrich, typical M_w = 55 000), ethylene glycol (VWR, H_2O > 0.02%), acetone (Pharmco Aaper, HPLC-UV grade), ethanol (Pharmco Aaper, 200 proof), and γ-Al_2O_3 (Alfa Aesar, 99.97% metal basis) were purchase and used as received.

The colloidal suspensions described below were diluted with acetone and centrifuged at 6000 rpm using a Hermle Z 300. The supernatants were clear. The precipitates were washed with acetone and acetone−ethanol mixture upon sonication using a Fisher Scientific FS30H sonicator bath. The cycles of dilution by acetone−ethanol mixtures, sonication, and centrifugation were repeated 4−5 times. The precipitates were dried in open air prior to characterization.

A Bruker C2 Discover (Parallel Beam) General Area Diffraction Detection (GADDS) system was used for measurement of powder diffraction profiles. A monochromatic Cu Kα radiation source (40 mV and 40 mA) was employed along with a Bruker ACS Hi-Star detector. The diffraction patterns were acquired between 33° and 90° by integrating four frames with 14° 2θ per frame. The samples were oscillated in the *xy* axis to homogenize the diffracting grains. Powder diffraction patterns were simulated using the DISCUS software package.[12] The ATOMS program was used to generate the spherical core/shell nanoclusters of desired Rh core sizes and Pt shell thicknesses. Fractional atom coordinates in a P_1 cubic lattice of 100 Å cell size were simulated using the Debye function with no symmetry constraints. Details of the simulations are given in the Supporting Information.

For the IR-CO probe experiments the colloidal solutions of the desired nanoparticle architectures were saturated with CO using a stainless steel needle submerged in the solution and bubbling CO at a flow rate between 20 and 40 sccm for ca. 20 min. A 100 μL aliquot of CO-saturated colloidal solution was transferred into a liquid IR cell and monitored in a Nexus 870 FT-IR spectrometer. The liquid IR cell consisted of a 0.5 mm Teflon spacer sandwiched between two rectangular-shaped CaF_2 windows. The colloidal solution prior to CO saturation was used for the background spectra.

A Renishaw Raman Microscope was employed to measure the micro-Raman spectra of CO-saturated nanoparticles. The nanoparticle powders were dispersed on glass slides and then sealed in a gastight Linkam temperature control stage. A 632.8 nm He:Ne or 488 nm Ar ion laser was focused on the particles through 0.5 mm quartz window using Leica N plan L50×/0.50 objective lens. The backscattered light was monitored with a resolution of 20 exposures/s between 300 and 2400 cm^{-1}. The particles were dosed with CO or CO/air mixtures for ca. 20 min. The spectra were recorded under flowing gas streams. Both 488 and 633 nm lasers yielded spectra with identical peak positions but different peak intensities. Only the 633 nm data are presented here.

TEM samples were prepared directly from the reaction solutions by diluting 20 μL of colloids to ~2 mL with deionized water. A 3 μL amount of such mixtures were drop cast and dried on continuous carbon film-deposited copper grids. A JEM 2100 LaB6 TEM operating at 200 kV was used for both low- and high-resolution imaging. A Jeol 2100F Field Emission Transmission Electron Microscope (FE-TEM) equipped with an Inca Energy Dispersive Spectrometer (EDS) was used for line scans and point spectra of nanoparticles. The FE-TEM was operated at 200 kV and in the scanning mode.

The catalysts were prepared by adding γ-Al_2O_3 to colloidal suspensions of nanoparticles and drying the slurry under vacuum. In a typical preparation, 10 mL of Rh@Pt nanoparticle colloidal suspension and 973 mg of γ-Al_2O_3 were mixed overnight and vaccuum dried at ca. 100 °C while vigorously stirring. Such composition yielded a 1.0% by weight Pt alumina-supported catalyst. The catalyst was washed with acetone several times with equivolume mixtures of acetone and ethanol and then baked at 60 °C overnight. Catalysis runs were carried out using 105 mg of catalyst charges in all cases. A standard fixed bed flow-through reactor was employed and has been described elsewhere.[11,13,14] An inlet velocity for gases of 0.21 m/s and a total flow rate of 400 NmL/min was employed. The gas hourly space velocity (GHSV) was calculated to be 2.3×10^5 mL g^{-1} h^{-1} with a corresponding residence time of ca. 35 ms. The gas mixture for the PROX reaction was composed of 0.2% CO (99.5% pure, Al tank), 0.5% O_2 (99.999% pure), 50% H_2 (99.999% pure), and the balance Ar (99.999% pure). Catalytic performance was evaluated by way of temperature-programmed reactions (TPR) between room temperature and 200 °C with a heating ramp rate of 1.8 °C/min. The gases were introduced to the reactor using carefully calibrated mass flow controllers. The gas products were monitored online using a Prima δB mass spectrometer. Supported catalysts were used "as prepared" and cycled through several TPR PROX runs (1−5 times) to attain optimal activity.

Synthesis. 2.7 nm Rh NPs. (1) Method 1. In a typical synthesis, 33.0 mg of $Rh(NO_3)_3 \cdot 2H_2O$ was dissolved in 20 mL of ethylene

(10) Park, J. Y.; Zhang, Y.; Grass, M.; Zhang, T.; Somorjai, G. A. *Nano Lett.* **2008**, *8*, 673–677.
(11) Alayoglu, S.; Nilekar, A. U.; Mavrikakis, M.; Eichhorn, B. *Nat. Mater.* **2008**, *7*, 333–338.
(12) Proffen, T.; Neder, R. B. *J. Appl. Crystallogr.* **1997**, *30*, 171–175.
(13) Zhou, S. G.; McIlwrath, K.; Jackson, G.; Eichhorn, B. *J. Am. Chem. Soc.* **2006**, *128*, 1780–1781.
(14) Zhou, S. H.; Jackson, G. S.; Eichhorn, B. *Adv. Funct. Mater.* **2007**, *17*, 3099–3104.

glycol (EG) in a 50 mL 3-neck round-bottom flask along with 28.0 mg of PVP_{55000}. The Rh^{3+} precursor salt was loaded in a dry box; all other transfers were done on a Schlenk line under N_2 atmospheres. The mixture was heated to ~80 °C and kept isothermal 10−15 min to dissolve the contents of the reaction mixture. The light brown solution was brought to boil in EG and refluxed for ca. 90 min. in flowing N_2 with vigorous stirring. The solution turned black and colloidal at about 110 °C. The reaction was quenched over ice. The colloids are stable for months without any precipitation.

(2) Method 2. In a typical reaction, 53.3 mg of $RhCl_3$ and 56.0 mg of PVP_{55000} were dissolved in 10 mL of EG in a 50 mL 2-neck round-bottom flask at 80 °C in flowing N_2. In a separate 100 mL 3-neck flask 30 mL of EG was heated to 100 °C in flowing N_2. Approximately 40 mg of granular $NaBH_4$ was then added into hot EG, and the mixture was heated to ~150 °C. The 80 °C $RhCl_3$ solution was then syringed into the 150 °C $NaBH_4$ solution. The resulting mixture instantly turned black colloidal and was refluxed for about 90 min in flowing N_2. The reaction was quenched on ice. Rh NPs colloids are stable for months without any precipitation.

5.7 nm Pt NPs. In a typical synthesis, 54.0 mg of $PtCl_2$ and 55.0 mg of PVP_{55000} in 40 mL of EG were refluxed for 1 h. To prepare the physical mixture, the monometallic colloidal suspensions of Pt and Rh NPs were mixed and stirred overnight.

3.3 and 3.9 nm Rh NPs. Typically, 20.3 mg of $RhCl_3$ was dissolved in 8 mL of Rh NP colloidal suspension (see Method 1 above) and diluted to 16 mL with EG. The mixture was heated to 80 °C in flowing N_2 to fully dissolve the $RhCl_3$. The mixture was then heated to 130 °C and aged for 4.5 h at 130 ± 2 °C. The reaction was quenched by immersing the flask in an ice bath, yielding 3.3 nm Rh NPs. Larger 3.9 nm Rh NPs were synthesized as described above, except 41.0 mg of $RhCl_3$ was dissolved in 16 mL of EG and mixed with 8 mL of Rh colloidal suspension (Method 1) and the mixture was aged at 130 ± 2 °C for 4 h.

2.2 nm PVP-Free Rh NPs. A 49.0 mg amount of $Rh(NO_3)_3 \cdot 2H_2O$ and 15.4 mg of $Rh_2(CO)_4Cl_2$ were transferred into a 50 mL 2-neck round-bottom flask in a dry box. The precursor salts were dissolved in 22.5 mL of EG on a Schlenk line under positive N_2 pressure. The solution was slowly brought to a boil and aged over 90 min with vigorous stirring. The reaction was quenched over ice. Some degree of aggregation/precipitation occurred after the reaction was quenched, but the colloidal suspension was restored with stirring.

2.2 nm PVP-Free Pt NPs. A 126.1 mg amount of H_2PtCl_6 was dissolved in 22 mL of EG. The yellow solution was slowly ramped to 130 °C and aged for 90 min to give a give a black colloidal suspension. The colloidal suspension of Pt NPs was aged for an additional 30 min at 180 °C and then quenched in an ice bath. The colloids were not stable in suspension and precipitated after 2 h at room temperature.

3.2 nm Rh@Pt NPs with 1 ML Thick Pt Shells. In a typical synthesis, 14.0 mg of $PtCl_2$ was dissolved in 10 mL of 2.7 nm Rh NP colloidal suspension and charged with an additional 10 mL of EG. The mixture was stirred at ~60 °C to dissolve the $PtCl_2$. The solution was brought to 130 °C with a temperature ramp of ~2 °C/min and aged for 4 h. The reaction was quenched over ice. The Rh@Pt nanoparticle colloids were not stable in solution and precipitated after 24 h.

5.1 nm Rh@Pt NPs with 2 ML Thick Pt Shells. In a typical reaction, 47.1 mg of $PtCl_2$ was dissolved in 10 mL of EG. A 10 mL amount of 3.9 nm Rh NP colloidal suspension was then added under flowing N_2 atmosphere at room temperature. The mixture was heated to 80 °C to ensure dissolution of the $PtCl_2$. The temperature was then ramped to 130 °C at a ramping rate of ~1 °C/min. The mixture was aged at 130 ± 3 °C for 4.5 h and then quenched to room temperature in an ice bath.

4.4 nm Rh@Pt NPs with 1 ML Thick Pt Shells. A 17.7 mg amount of $PtCl_2$ was dissolved in 10 mL of EG. A 10 mL amount of 3.9 nm Rh NPs suspension was added. Finally, the mixture was ramped to 130 °C with a heating rate of 1−2 °C/min and aged for 4 h. The colloidal suspension was quenched in an ice bath.

4.3 nm Rh@Pt NPs with 2 ML Thick Pt Shells. A 27.8 mg amount of $PtCl_2$ was dissolved in 10 mL of EG, and 10 mL of 3.3 nm Rh NPs suspension was added as described above. Pt was deposited at 130 °C. The colloidal suspension was quenched in an ice bath after 4 h of aging.

2.7 nm PVP-Free Rh@Pt NPs with ca. 1 ML Thick Pt Shells. The same procedures were used as described above, except the 2.2 nm PVP-free Rh colloids were used, the deposition temperature was 130 °C, and the deposition time was 2 h. A slow temperature ramp of ~1 °C/min was employed for Pt deposition. The PVP-free colloids were stable for only short periods of time and precipitate over 2 h unless stirred.

PtRh (1:1) Alloy NPs. A 40.0 mg amount of $Pt(acac)_2$ and 19.6 mg of $Rh_2(CO)_4Cl_2$ salts were dissolved in 20 mL of EG along with 55.0 mg of PVP_{55000}. The temperature was ramped to a boil in less than 10 min. The solution turned black colloidal at about 170 °C. The colloidal suspension was refluxed for about 2 h and quenched over ice.

Results

In this study, monometallic NPs of Rh and Pt were prepared by modifications of known polyol methods.[15] The Rh NPs were used directly in catalytic evaluations and also as the core "seeds" in the preparation of Rh@Pt core−shell particles. Uniform 2.7 nm Rh NPs were prepared by reducing $Rh(NO_3)_3 \cdot 2H_2O$ in ethylene glycol in the presence of PVP stabilizers. Changing the temperature and/or PVP:Rh ratio did not significantly affect the resulting NP sizes or size distributions. A second method for making 2.7 nm Rh NPs from $RhCl_3$ was also employed to make catalysts and seeds for subsequent growth studies. While both methods gave NPs that were structurally and spectroscopically identical, the $RhCl_3$ method produced superior catalysts. Chloride or other impurities were not detected by EDS in any of the Rh NPs. To prepare larger Rh NPs, a sequential growth method was employed in which additional Rh layers were deposited over preformed Rh seeds at temperatures that did not favor self-nucleation. The procedure is similar to that described by Somorjai and Tilley but with different precursors and less PVP.[16,17] The less oxidizing $RhCl_3$ precursor was used for the sequential growth step. By controlling the stoichiometry, uniform Rh NPs of 3.3 or 3.9 nm were prepared. Representative TEM images and particle size histograms are found in Figures 1a and S1, Supporting Information.

Pt shells were deposited on the Rh seeds to generate Rh@Pt core−shell NPs using a $PtCl_2$ precursor and similar seeded growth techniques.[18] To achieve a desired shell thickness the $PtCl_2$ concentrations were adjusted to accommodate the size of the Rh core particles. The stoichiometric ratios were calculated by employing a modified form of Schmid's Magic Number algorithm for cubeoctahedral clusters and the density of the FCC metal (see Table S1, Supporting Information).[19−22] The Pt shells

(15) He, B. L.; Chen, Y. X.; Liu, H. F.; Liu, Y. *J. Nanosci. Nanotechnol.* **2005**, *5*, 266–270.
(16) Humphrey, S. M.; Grass, M. E.; Habas, S. E.; Niesz, K.; Somorjai, G. A.; Tilley, T. D. *Nano Lett.* **2007**, *7*, 785–790.
(17) Hoefelmeyer, J. D.; Niesz, K.; Somorjai, G. A.; Tilley, T. D. *Nano Lett.* **2005**, *5*, 435–438.
(18) Lima, F. H. B.; Gonzalez, E. R. *Appl. Catal. B: Environ.* **2008**, *79*, 341–346.
(19) Schmid, G. *Nanostruct. Mater.* **1995**, *6*, 15–24.
(20) Schmid, G. *Chem. Rev.* **1992**, *92*, 1709–1727.
(21) Martin, T. P.; Bergmann, T.; Gohlich, H.; Lange, T. *J. Phys. Chem.* **1991**, *95*, 6421–6429.
(22) Aiken, J. D.; Finke, R. G. *J. Mol. Catal. A: Chem.* **1999**, *145*, 1–44.

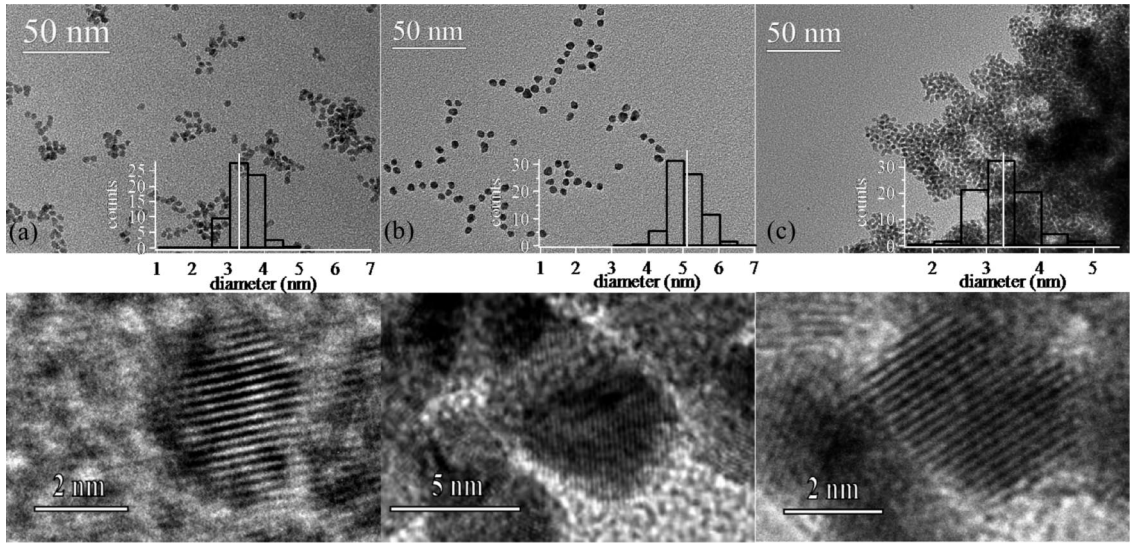

Figure 1. Representative TEM images of (a) 3.3 nm Rh NPs prepared by sequential deposition, (b) PVP-stabilized 5.1 nm Rh@Pt core/shell NPs comprising 3.9 nm Rh cores and 2 ML Pt shells, and (c) PVP-free 3.3 nm Rh@Pt core/shell NPs comprising 2.2 nm Rh cores and 2 ML Pt shells. High-resolution images of the particles in a−c are shown directly below each figure.

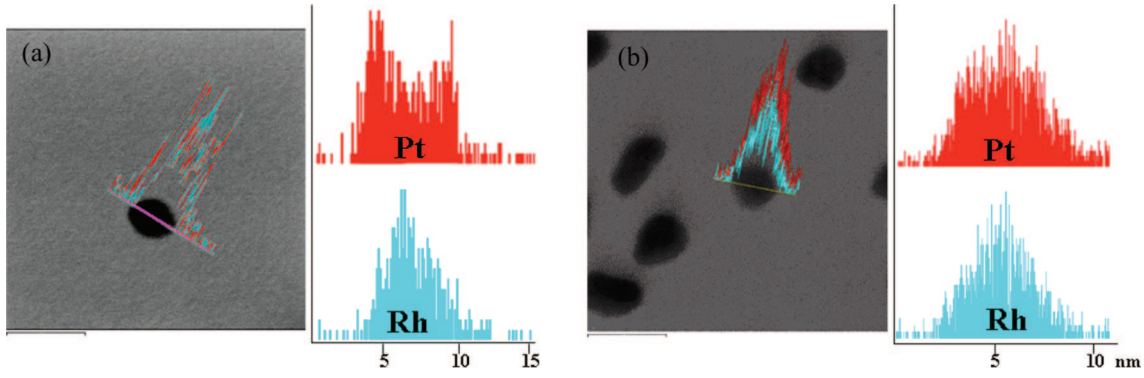

Figure 2. Representative STEM-EDS line spectra of (a) a 5.1 nm Rh@Pt NP with 3.9 nm Rh core and 2 ML Pt shell and (b) a 5 nm PtRh alloy nanoparticle. Relative atomic % composition (vertical axis) of Pt (red) and Rh (blue) are plotted against the line scan probe position (horizontal axis) and given next to STEM images. A 1.5 nm probe was used to trace 10−15 nm scans across each particle. The particle center is at ∼6.5 nm in a and ∼ 5.5 nm in b.

were also deposited at under-nucleation temperatures to avoid self-nucleation of monometallic Pt NPs. Aging the colloidal solutions up to 3−4 h was required to guarantee clear/colorless supernatants with no $PtCl_2$ deposits. Rh@Pt NPs were selectively prepared from 2.7, 3.3, and 3.9 nm Rh cores with ∼1 and ∼ 2 ML Pt shells. Representative TEM images and particle size histograms are found in Figures 1b and S1, Supporting Information. The size evolutions of the core−shell particles are in agreement with the calculated shell thicknesses and thus agree well with expectations based on the Schmid model. While CO probe experiments show that the core Rh particles are completely encapsulated by the Pt shells (see below), the monolayer coverages described here will certainly have variations from particle to particle due to core size dispersity and are only intended to represent mean values. After Pt deposition the colloids persisted for ca. 24 h and then began to agglomerate and deposit on the bottom of the flask.

$Pt_{1-x}Rh_x$ alloy NPs were prepared by coreduction of $Pt(acac)_2$ and $Rh_2(CO)_4Cl_2$ in EG solutions with PVP stabilizers.[10,23,24] We found that these precursors gave the most homogeneous alloy structures and avoided monometallic particle contaminates and the graded alloy formation produced from other methods. TEM analysis shows 4.9 nm particles but some shape anisotropy (see Figure S3, Supporting Information).

PVP-free samples of Rh and Rh@Pt NPs were also prepared using different precursors and slightly different protocols. The resulting particles had mean sizes and size distributions similar to the PVP analogs but the particles agglomerated (see Figures 1c and S2, Supporting Information) and the colloids persisted for short time periods (ca. 1−2 h) before deposition as expected.

The NPs described above have been fully characterized by a combination of TEM, single-particle EDS, EDS line scans, XRD analysis, FT-IR, and micro-Raman CO probe experiments and catalytic evaluation. These experiments are described below.

The composition and architecture (core−shell vs alloy) of individual NPs were evaluated using a 1.5 nm EDS probe in a JEOL 2100 FE TEM operating in the STEM mode. Multiple single-particle EDS analysis of core−shell and alloy NPs from various syntheses confirmed that all particles are bimetallic in nature, and stray monometallic particles were not observed in any of the samples. STEM-EDS line scans were recorded from 5.1 nm Rh@Pt NPs containing 2 ML Pt shells (Figure 2a). The data clearly show the Pt M line with a bimodal Pt distribution

(23) Bergounhou, C.; Blandy, C.; Choukroun, R.; Lecante, P.; Lorber, C.; Pellegatta, J. L. *New J. Chem.* **2007**, *31*, 218–223.
(24) Harada, M.; Einaga, H. *J. Colloid Interface Sci.* **2007**, *308*, 568–572.

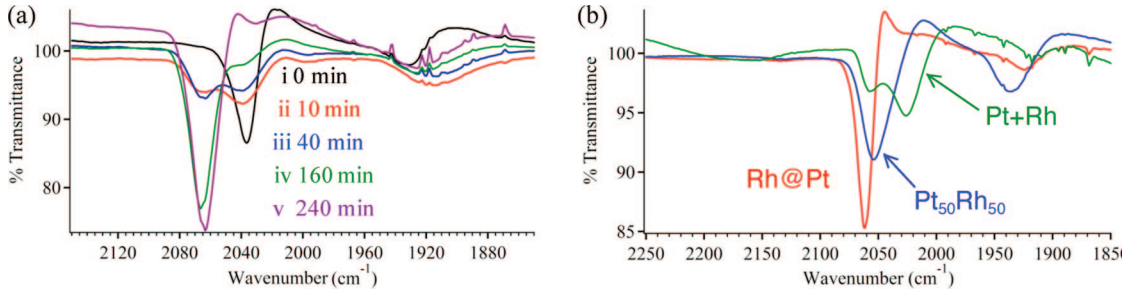

Figure 3. (a) Ex-situ FT-IR spectra of CO-saturated colloidal suspensions sampled as a function of time during synthesis of the Rh@Pt NPs. The stacked plots show (i) parent Rh core NPs at 0 min and (ii) Rh@Pt NPs in 10th min, (iii) 40th min, (iv) 160th min, (v) and 240th min. (b) FT-IR spectra of CO-saturated colloidal suspensions comparing core−shell (red), 50:50 alloy (blue), and a mixture of monometallic Rh and Pt nanoparticles (green).

that reaches a maximum at the edge of the particle (i.e., the shell), whereas the Rh L line shows maximum Rh concentration at the center of the particle. STEM-EDS point spectra acquired from different regions of a distinct nanoparticle show the highest atomic % Pt at the edge with more atomic % Rh at the center (Figure S4, Supporting Information), which is consistent with the EDS line scan. In contrast, the PtRh alloy NPs show single Gaussian distributions of X-rays across the particle for both elements as expected from the random arrangement of atoms (Figure 2b). Definitive EDS line scan spectra could not be obtained for the 3−4.5 nm Rh@Pt NPs due to limitations of the 1.5 nm probe size. However, correlations of XRD and CO probe experiments (see below) show that the smaller core−shell particles have the same structure.

To evaluate the surface structures of the various NPs we employed CO-probe experiments[25−27] as a qualitative tool to differentiate Pt from Rh on the surface of the particles. CO is a well-known and long-studied molecular probe and particularly convenient to monitor by FT-IR and micro-Raman spectroscopy. The core/shell architecture with only one type of surface atom can qualitatively be distinguished from other bimetallic architectures, namely, alloys and physical mixtures, which have both elements on the NP surface. CO-saturated colloidal Rh suspensions give rise to two features in their FT-IR spectra. The strong broad peak at 2034 cm^{-1} is assigned to CO in the atop position and the lower intensity band at 1940 cm^{-1} to bridging CO on Rh (see Figure 3). PVP-free Rh NPs have identical spectra. Gem dicarbonyl modes were not observed in any of our colloidal Rh NPs.[28−30]

The CO-probe technique has been used to spectroscopically monitor formation of the Pt shell in the synthesis of the Rh@Pt NPs. The colloidal solutions were sampled at various times in the reaction, saturated with CO, and evaluated by FT-IR (Figure 3). The υ(CO) bands associated with the Rh NPs decrease in intensity as the terminal and bridging CO bands associated with CO sorbed to Pt surfaces emerge. After 4 h of reaction CO bands associated with exposed Rh surfaces have disappeared and only Pt−CO modes are observed. Assuming that the incomplete Pt shell exists as small islands on the Rh core at short reaction times, the FT-IR data suggest that the sorbed CO on the two surfaces are not strongly coupled and give rise to separate υ(CO) modes. This observation is in contrast to spectra for the PtRh alloy NP colloids that show a single, atop υ(CO) peak that is intermediate to those on monometallic Pt and Rh (Figure 3b). Importantly, the core−shell architecture is conveniently distinguished from both the alloy and the monometallic rhodium phases by FT-IR CO probe experiments. As the Rh cores increase in size and/or thicker Pt shells are deposited, the Rh@Pt atop mode is blue shifted from 2061 to 2073 cm^{-1} but is always distinct from the alloy atop υ(CO) mode, which appears at 2055−2058 cm^{-1}. As such, the IR experiments provide a connection between small particles for which TEM line scans are not possible and the larger particles where line scans clearly distinguish the core−shell architecture from the alloy. The blue shift of the atop mode may be due to differential faceting of the Pt shell as the particles become larger or lateral effects associated with altered equilibrium CO coverages. Interestingly, the FT-IR spectra for the PVP-free Rh@Pt core−shell NPs are virtually identical to those of PVP-protected particles (Figure S6b, Supporting Information), suggesting that PVP does not significantly affect the equilibrium CO coverage or the electronic structure of the surface.

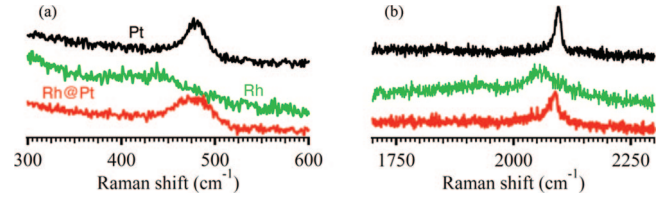

Figure 4. Micro-Raman (633 nm) spectra of CO-saturated PVP-free NPs showing (a) the υ(M−C) region (M = Pt, Rh) and (b) the υ(CO) region. The data were recorded for 2.2 nm Pt NPs (black), 2.2 nm Rh NPs (green), and 2.7 nm Rh@Pt NPs (red) in 2.5:1 air-to-CO gas mixtures.

Micro-Raman spectra of Rh@Pt, Rh, and Pt NPs saturated with CO are shown in Figure 4. Raman analyses of PVP-coated NPs were not extensively studied due to formation of PVP-derived graphite-like deposits[37] that diminish CO signal intensities and obscure the M−C regions of the spectrum. The Raman data described below were collected from PVP-free samples under flowing CO atmospheres. Maximum peak intensities were observed with 2.5:1 air:CO gas mixtures, but the peak positions were the same in pure CO. Peaks in both regions of the spectrum disappeared when the CO atmospheres were removed. Monometallic Pt NPs give rise to two peaks, namely, a sharp peak at 2095 cm^{-1} assigned to υ(CO) on atop Pt sites and a broader 480 cm^{-1} peak due to the υ(Pt−C) mode (Figure 4). Similarly, Rh NPs give rise to two υ(CO) features at 2060 and ∼1920

(25) Wang, Y.; Toshima, N. *J. Phys. Chem. B* **1997**, *101*, 5301–5306.
(26) Dassenoy, F.; Casanove, M. J.; Lecante, P.; Pan, C.; Philippot, K.; Amiens, C.; Chaudret, B. *Phys. Rev. B* **2001**, *63*, 235407/1–235407/7.
(27) Pan, C.; Dassenoy, F.; Casanove, M. J.; Philippot, K.; Amiens, C.; Lecante, P.; Mosset, A.; Chaudret, B. *J. Phys. Chem. B* **1999**, *103*, 10098–10101.
(28) Pasztor, M.; Solymosi, F. *Magy. Kem. Foly.* **1986**, *92*, 321–328.
(29) Vantblik, H. F. J.; Vanzon, J. B. A. D.; Huizinga, T.; Vis, J. C.; Koningsberger, D. C.; Prins, R. *J. Am. Chem. Soc.* **1985**, *107*, 3139–3147.
(30) Siepen, K.; Bonnemann, H.; Brijoux, W.; Rothe, J.; Hormes, J. *Appl. Organomet. Chem.* **2000**, *14*, 549–556.

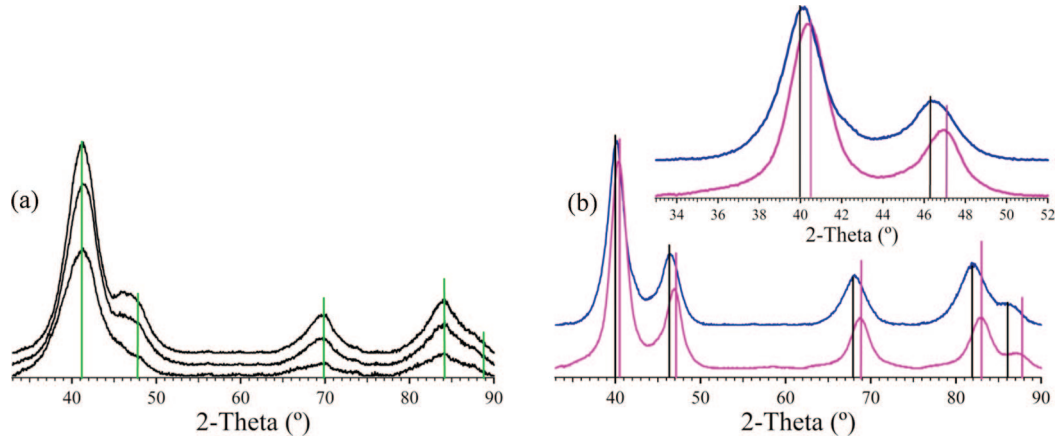

Figure 5. XRD profiles comparing (a) Rh NPs via polyol reduction of $Rh(NO_3)_3 \cdot 2H_2O$ to give (bottom) 2.7 nm as-synthesized Rh NPs, (middle) 3.3 nm Rh NPs, and (top) 3.9 nm Rh NPs grown from sequential deposition. (b) XRD profiles of Rh@Pt core−shell (blue pattern) and (1:1) PtRh alloy (purple pattern) NPs of similar particle diameters. The inset shows an enlargement of the 111 and 200 reflections. JCPDS lines for Pt (black), Rh (green), and 1:1 PtRh alloy (purple) are also shown.

cm^{-1} for linear atop CO and bridging CO, respectively. In addition, a very broad 440 cm^{-1} peak for the υ(Rh−C) mode is present. The Rh@Pt core−shell NPs yield features that are characteristics of Pt surfaces, namely, broadened peaks at 2090 and 480 cm^{-1}, which are assigned to linear υ(CO) and υ(M−C) bands, respectively, and may be indicative of electronically altered Pt surfaces.

Powder X-ray diffraction analysis (XRD) coupled with Debye function simulations (DF) provides an effective means of differentiating alloys from core−shell NPs and monitoring shell growth in multilayer particles. Powder diffraction profiles of as-made 2.7 nm Rh NPs exhibit strong broad 111 reflections centered ca. 41° (Figure 5a). The 200 reflection and other high-angle peaks are weak, but metallic Rh is evident. Figure 5a shows that crystallinity increases with increasing size of the Rh NPs; however, the peaks remain broad and denote disorder. The core−shell and alloy NPs of identical composition and similar size are easily differentiated by their XRD patterns (Figure 5b).

XRD analyses of core−shell particles are hindered by similarities of the FCC unit cells of the two metals (Pt, a = 3.916 Å; Rh, a = 3.814 Å). However, discernible shifts in peak positions in both experimental and simulated diffraction patterns provide nonintuitive insight into the diffraction behavior of core−shell bimetallic NP structures. In particular, the data show that (1) the diffraction patterns are dominated by the thin (1−3 ML) Pt shells, (2) shifts in the XRD profiles can be accurately described through DF simulations, and (3) DFA/XRD analysis can be used to evaluate changes in shell thicknesses in particles having the same core size. These findings are described below.

The Rh@Pt NPs all show a single 111 FCC peak centered at ca. 40° for which distinct Pt and Rh phases cannot be discerned due to the inherent broadness of the diffraction patterns (Figure 6a). While the peak positions of the Rh@Pt core−shell particles are dominated by Pt diffraction, the peaks shift toward Rh peak positions as the mass % Rh increases. For example, as the Rh cores become larger with Pt shells of the same size, the diffraction peaks shift toward those of bulk Rh. Likewise, as the Pt shell thickness is increased on Rh cores of the same size the diffraction peaks shift further toward those of bulk Pt. In certain cases, such as the 4.4 nm Rh@Pt NPs comprising 3.9 nm Rh cores and 1 ML thick Pt shells, the XRD patterns approach the peak positions of the bulk (1:1) PtRh alloy phase (see light blue profile in Figure 6a). However, this shift does not result from PtRh alloy formation but instead is a consequence of mass-averaged diffraction effects associated with the core−shell structure. The IR CO-probe data for these 4.4 nm Rh@Pt NPs clearly show a pure Pt surface and are inconsistent with alloy formation (see Figure S5, Supporting Information). To further illustrate this point we performed Debye function (DF) simulations of model core−shell systems generated from idealized spherical particles of FCC metals with the desired core and shell configurations.[31−33] Details of the models are given in the Supporting Information. The simulated powder diffraction patterns were calculated from nondistorted model particles using the DF sub-routine in the DISCUS software package.[12] The simulations are shown in Figure 6b and qualitatively show systematic peak shifts toward higher angles as the core size increases and/or the shell thickness decreases. For example, two Rh@Pt NPs with 3.9 nm Rh cores are shown in Figure 6. Those particles with 2 ML Pt shells (dark blue) show diffraction peaks that are almost perfectly aligned with bulk Pt, whereas those with 1 ML Pt shells (light blue) are noticeably shifted toward Rh peak positions in both the simulated and the observed XRD patterns. The *quantitative* differences in peak positions most likely result from lattice distortions (primarily in the shell) associated with the pseudoepitaxial growth of thin Pt shells on the particle cores.

As in other core−shell and alloy NP systems multiple analytical methods are required to fully characterize and differentiate the different architectural configurations. While STEM-EDS line scans shown in Figure 2 clearly differentiate the 5.1 nm Rh@Pt core−shell NPs from the 4.9 nm (1:1) PtRh alloy NPs, the smaller catalytically relevant NPs cannot be evaluated through line scans due to limitations of the probe size. However, the micro-Raman data and comparisons of IR-CO probe experiments and XRD data show that the small particles have the same core−shell architectures as the larger particles evaluated in Figure 2. Moreover, the activities of the core−shell and alloy particles are distinguished in the catalytic evaluations described below.

(31) Bonnemann, H.; Britz, P.; Vogel, W. *Langmuir* **1998**, *14*, 6654–6657.
(32) Reetz, M. T.; Winter, M.; Breinbauer, R.; Thurn-Albrecht, T.; Vogel, W. *Chem. Eur. J.* **2001**, *7*, 1084–1094.
(33) Vogel, W. *Cryst. Res. Technol.* **1998**, *33*, 1141–1154.

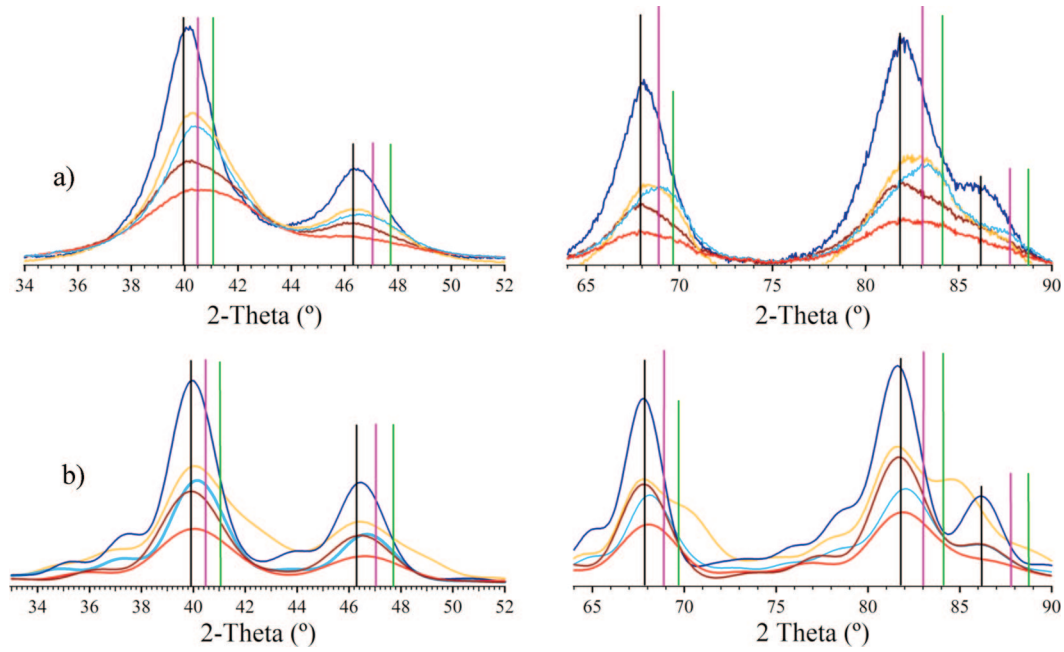

Figure 6. (a) XRD profiles and (b) DFA simulations of Rh@Pt NPs of various core diameters and shell thicknesses: (red) 2.7 nm Rh core, 1 ML Pt shell; (reddish brown) 2.7 nm Rh core, 2 ML thick Pt shell; (light blue) 3.9 nm Rh core, 1 ML Pt shell; (orange) 3.3 nm Rh core, 2 ML Pt shell; (dark blue) 3.9 nm Rh core, 2 ML Pt shell. JCPDS peak positions for Pt (black), 1:1 RhPt alloy (purple), and Rh (green) are also presented.

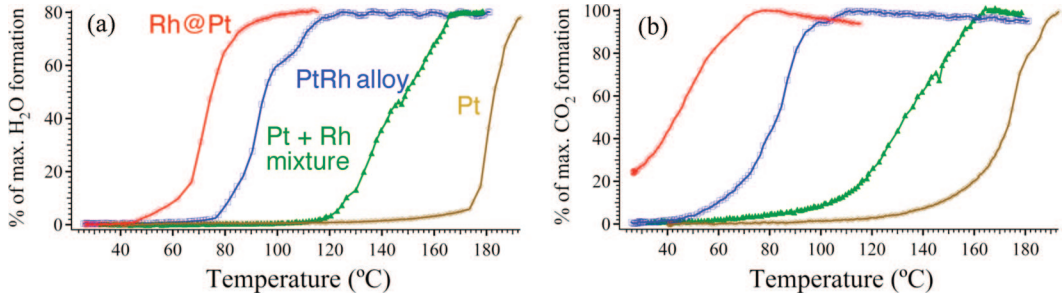

Figure 7. TPR plots showing (a) H_2O formation and (b) CO_2 formation for monometallic Pt NPs, monometallic mixtures of Pt NPs, and 2.7 nm Rh particles, 4.9 nm $Pt_{50}Rh_{50}$ alloy NPs, and 3.2 nm Rh@Pt NPs for H_2 streams contaminated with 2000 ppm CO. Percent of maximum H_2O formation was calculated from the limiting reactant, O_2, and % of maximum CO_2 formation is relative to the CO inlet concentration. See text for details.

To compare and contrast the activity of the core−shell NPs with that of the alloys and monometallic NPs we evaluated the PROX reaction (preferential oxidation of CO in H_2) using H_2 feeds contaminated by 0.2% CO by volume along with 0.5% O_2. The Pt−Rh catalysts were supported on γ-Al_2O_3, and each were loaded with 1.0 wt % Pt and equimolar Pt:Rh ratios. The reactions were conducted in a fixed-bed, flow-through reactor, and catalytic activity was monitored by way of temperature-programmed reactions (TPR) measuring the evolution of H_2O and CO_2. The results are shown in Figure 7. The maximum CO_2 formation (100% in Figure 7) is based on the 0.2% inlet CO concentration. The maximum H_2O formation was calculated from the limiting reactant O_2, so that 100% H_2O formation would result in conversion of all O_2 to water. Using the gas mixtures described above, complete conversion of CO to CO_2 followed by hydrogen oxidation with the remaining O_2 would result in an 80% H_2O formation.

The TPR data for the core−shell Rh@Pt NPs with ca. 1 ML thick Pt shells, (1:1) PtRh alloy NPs, and monometallic mixtures of Pt and Rh NPs are shown in Figure 7. In general, CO oxidation significantly precedes H_2 oxidation for the core−shell and alloy catalysts, which gives rise to high PROX selectivities at relatively low temperatures. For the four different batches of Rh@Pt catalysts the temperature for complete CO conversion varied from 60 to 90 °C with H_2 light-off varying from 35 and 60 °C (see Supporting Information, Figure S7). In contrast, CO and H_2 oxidation occur almost simultaneously for the monometallic mixture, which gives very poor PROX selectivities along with low activities. For reference, our pure Pt NP catalysts under these conditions show CO and H_2 oxidation onsets (light off) at 155−160 and 175−180 °C, respectively, which is consistent with literature reports.[34] While the monometallic mixture of Rh + Pt shows somewhat better PROX activity (160 °C complete CO oxidation) than that of pure Pt (190 °C complete CO oxidation), it is far less active than the PtRh alloy (105 °C complete CO oxidation) or Rh@Pt core−shell (70 °C complete CO oxidation) catalysts under identical conditions and loadings (Figure 7). In particular, the best Rh@Pt core−shell NP catalyst shows complete CO oxidation by 40 °C and a subsequent H_2 oxidation that is complete by 80 °C with exceedingly high PROX selectivity at room temperature (see Figure S7, Supporting Information). However, a representative catalyst with activity that is intermediate in the four independent

(34) Minemura, Y.; Ito, S.; Miyao, T.; Naito, S.; Tomishige, K.; Kunimori, K. *Chem. Commun.* **2005**, 1429–1431.

Table 1. Comparative PROX Selectivities[a] for the Different Rh−Pt and Ru@Pt Core/Shell[b] Catalysts

	$T_{50\pm5}(O_2)$,[c] °C	selectivity[d] at $T_{50\pm5}$	$T_{50\pm5}(CO_2)$,[e] °C	selectivity[d] at $T_{50\pm5}$	$T_{comp\pm0.1}(O_2)$,[f] °C	selectivity[d] at $T_{comp\pm1}$
Ru@Pt (1:1)	66 ± 4	74 ± 3	45 ± 4	83 ± 1	178 ± 3	40.4 ± 0.4
Rh@Pt (1:1)	79 + 4	90 ± 3	65 ± 3	95.6 ± 0.4	136 ± 1	49.7 ± 0.1
Rh@Pt (1:2)	44 ± 6	99.8 ± 0.1	33 ± 4	99.6 ± 0.3	122 ± 1	48.3 ± 0.1
Pt + Rh	163	76	162 ± 3	79 ± 1	192 ± 7	47.0 ± 0.5
$Pt_{50}Rh_{50}$	174 ± 6	55.2 ± 0.4	176 ± 3	55.2 ± 0.1	215 ± 3	46.2 ± 0.3

[a] PROX feed is composed of 1% CO, 1% O_2, 50% H_2, and an Ar balance. [b] See ref 11. [c] Temperature of 50 ± 5% O_2 consumption. [d] Selectivity is defined as $[\chi_{CO2}/(\chi_{CO2} + \chi_{H2O})] \times 100$ where χ_{CO2} is the fraction of O_2 used to convert CO to CO_2 and χ_{H2O} is the fraction of O_2 used to convert H_2 to H_2O. [e] Temperature of 50 ± 5% CO conversion. [f] Temperature of complete (99.9 ± 0.1%) O_2 consumption. [g] Temperatures and selectivities were estimated due to abrupt light off (see Figures S8 and S9 in the Supporting Information for TPR data).

batches tested is shown in Figure 7 for comparison. A full analysis of the PROX activity under different conditions, comparisons with other core−shell particles, and a theoretical analysis of these systems will be described in a subsequent publication.

Discussion

Through the use of various precursors and protocols PtRh bimetallic nanoparticles with different architectures (i.e., core−shell, alloy, and mixtures of monometallic NP) can be prepared selectively. Combinations of analytical techniques are required to identify and characterize the different configurations, especially for small bimetallics where EDS line scans are not feasible. The complete architectural series of Rh and Pt bimetallic NPs represents the third such complete series along with the PtAu[13,14] and PtRu[11] systems. While the sizes, compositions, and projected surface areas of the NPs within these three series are quite similar, the catalytic activities are markedly different. For both the PtRu and PtRh bimetallic systems the core−shell particles were most active for PROX followed by the alloys, the mixture of monometallic NPs, and finally the pure Pt NPs. The enhancements in activities are directly related to the changes in architectural configurations, which alter the electronic structures of the surface metals and/or facilitate alternate reaction mechanisms relative to pure Pt. However, the changes in activities for the different Rh−Pt architectures are less dramatic than the Ru−Pt systems,[11] but the PROX selectivities are better (see Table 1). Mavrikakis has shown[8,9] that core−shell particles containing Pt shells on Rh and Ru cores have lower equilibrium CO coverages and lower Pt−H bond enthalpies relative to pure Pt, which explains the enhancements in CO and H_2 oxidation kinetics. These differences in substrate binding are correlated with shifts in the Pt d-band center due to charge transfer between the Pt shell and the core metals. The situation is directly analogous to the thin film studies of Goodman and Campbell[5−7] in which electron transfer between metal overlayers and their metallic hosts altered the metal−metal interactions and surface electronic structures. The authors noted that the electronic charge transfer in the overlayer structures differed from that in the bulk alloys, suggesting that the Rh−Pt electronic interactions in Rh@Pt NPs and RhPt alloy NPs may also be different. In addition to possible differences in electronic structure, the alloy NPs also have two types of surface atoms and can therefore promote alternate mechanisms of reaction in which different atoms catalyze different steps (e.g., the bifunctional mechanism).[35,36]

A comparison of the PROX activities and selectivities for a 1% CO, 1% O_2, and 50% H_2 feed of the different Rh−Pt catalysts and the Ru@Pt catalyst[11] is given in Table 1. While the activities of the Rh@Pt NPs toward PROX are better than the RhPt alloy, the differences are not as dramatic as the Ru/Pt system.[11] Although it is clear that the Pt−Rh bimetallic particles have a clear synergistic effect for PROX activity, the enhancement of the core−shell structure is far less pronounced in the present case. However, the presence of room-temperature CO oxidation in all of the Rh@Pt systems tested and lack of such activity for the alloys clearly demarcates the differences in the architectures.

Finally, we note that PVP-free NPs of various architectures are easily accessible by the methods described herein; however, the stability of the colloids is limited, and the resulting particles show significant agglomeration (see Figure 1c). While the FT-IR CO probe data of the PVP-protected and PVP-free NPs are virtually identical, the Raman signals of the CO-saturated PVP-free NPs are significantly more intense. The lack of graphitic deposits associated with PVP degradation[37] may explain the gain in intensity of the latter. Catalytically, the PVP-free particles did not perform as well as the PVP-protected materials due to agglomeration.

Acknowledgment. This material is based upon work supported by the National Science Foundation under grant no. CHE0401850 and the DOE HFI program under grant no. DE-FG02-05ER15731. We thank Dr. Wen-An Chou for assistance with TEM data collection and gratefully acknowledge the NSF MRI for funding through grant 0619191.

Supporting Information Available: Additional TEM data and particle size histograms, core−shell synthetic charts, IR data, and details of the diffraction models. This material is available free of charge via the Internet at http://pubs.acs.org.

JA8061425

(35) Guo, Y. L.; Zheng, D. Q.; Liu, H. Y.; Friedrich, A.; Garche, J. *J. New Mater. Electr. Syst.* **2006**, *9*, 33–39.
(36) Roth, C.; Papworth, A. J.; Hussain, I.; Nichols, R. J.; Schiffrin, D. J. *J. Electroanal. Chem.* **2005**, *581*, 79–85.
(37) Borodko, Y.; Humphrey, S. M.; Tilley, T. D.; Frei, H.; Somorjai, G. A. *J. Phys. Chem. C* **2007**, *111*, 6288–6295.